# Simultaneous Rocket and Scintillation Observations of Plasma Irregularities Associated With a Reversed Flow Event in the Cusp Ionosphere

Yaqi Jin[1] , Jøran I. Moen[1,2] , Andres Spicher[1] , Kjellmar Oksavik[2,3] , Wojciech J. Miloch[1] , Lasse B. N. Clausen[1] , Mariusz Pożoga[4], and Yoshifumi Saito[5]

[1]Department of Physics, University of Oslo, Oslo, Norway, [2]Arctic Geophysics, University Centre in Svalbard, Longyearbyen, Norway, [3]Birkeland Centre for Space Science, Department of Physics and Technology, University of Bergen, Bergen, Norway, [4]Space Research Center, Polish Academy of Sciences, Warsaw, Poland, [5]Institute of Space and Astronautical Science, Japan Aerospace Exploration Agency, Sagamihara, Japan

**Abstract** We present an overview of the ionospheric conditions during the launch of the Investigation of Cusp Irregularities 3 (ICI-3) sounding rocket. ICI-3 was launched from Ny-Ålesund, Svalbard, at 7:21.31 UT on 3 December 2011. The objective of ICI-3 was to intersect the reversed flow event (RFE), which is thought to be an important source for the rapid development of ionospheric irregularities in the cusp ionosphere. The interplanetary magnetic field was characterized by strongly negative $Bz$ and weakly negative By. The EISCAT Svalbard radar (ESR) 32-m beam was operating in a fast azimuth sweep mode between 180° (south) and 300° (northwest) at an elevation angle of 30°. The ESR observed a series of RFEs as westward flow channels that were opposed to the large-scale eastward plasma flow in the prenoon sector. ICI-3 intersected the first RFE in the ESR field of view and observed flow structures that were consistent with the ESR observations. Furthermore, ICI-3 revealed finer-scale flow structures inside the RFE. The high-resolution electron density data show intense fluctuations at all scales throughout the RFE. The ionospheric pierce point of the GPS satellite PRN30, which was tracked at Hornsund, intersected the RFE at the same time. The GPS scintillation data show moderate phase scintillations and weak amplitude scintillations. A comparison of the power spectra reveals a good match between the ground-based GPS carrier phase measurements and the spectral slope of the in situ electron density data in the lower frequency range. It demonstrates the possibility of modelling GPS scintillations from high-resolution in situ electron density data.

## 1. Introduction

A reversed flow event (RFE) is a mesoscale flow structure in the cusp ionosphere, which refers to east-west elongated segments of the enhanced ion flow in the direction opposite to the background plasma flow (Rinne et al., 2007). RFEs are 100- to 200-km wide in latitude with an average lifetime of approximately 18 min. From the fast azimuth sweeps of the EISCAT Svalbard radar (ESR) in the winter cusp ionosphere, it was found that RFEs never formed simultaneously in pairs, and thus, they cannot be explained with the symmetric Southwood flux transfer event (FTE) model (Southwood, 1987). Instead, an asymmetric version of the Southwood FTE model, in which the RFE is interpreted as the return flow on the poleward side of the newly opened flux tube, was proposed by Rinne et al. (2007). Moen et al. (2008) studied the RFE in the context of ground-based auroral observations and found that the RFE onset is in concert with the brightening of a discrete arc near the open-closed field line boundary. A thin Birkeland current arc is located exactly at a sharp clockwise flow reversal, implying a converging electric field and an upward field-aligned current (FAC).

Given the spatial scale of the RFE (100–200 km in latitude), it is possible to observe the RFE with a high frequency (HF) radar by considering its spatial resolution. Oksavik et al. (2011) presented the first observations of the RFE seen by the Super Dual Auroral Radar Network (SuperDARN) HF radar. Broad Doppler spectral width was observed near the edges of RFEs. Using large flow shears in the RFE system, Oksavik et al. (2011) tested the growth rate of the Kelvin-Helmholtz instability (KHI) and found it can be fast enough to explain the fast irregularity onset in the cusp ionosphere. The large flow shears associated with the RFE led Carlson et al. (2007) to propose a two-step process to explain the observed rapid development of cusp irregularities. In this new framework, the KHI first works on the cusp-entering plasma to quickly produce mesoscale plasma

structures. Next, the gradient drift instability operates on these structures to produce smaller scale irregularities.

The cusp inflow region is crucial for the plasma intake from lower latitudes and for irregularity formation in the dayside polar cap (e.g., Carlson, 2012). The plasma irregularities near the cusp have been studied by using HF radars (Moen, Carlson, et al., 2001; Oksavik et al., 2011), GPS scintillation receivers (Jin et al., 2015, 2017, 2018; Oksavik et al., 2015), and in situ sounding rockets (Moen et al., 2012; Oksavik et al., 2012; Spicher et al., 2014, 2015, 2016).

In this paper, we focus on characterizing plasma irregularities associated with the RFE on 3 December 2011, by combining in situ ICI-3 sounding rocket and ground-based instruments. Both the ground-based GPS scintillation data and the in situ electron density data are widely used to study ionospheric irregularities (Basu et al., 1988; Kelley et al., 1980). The current study benefits from a very high-resolution electron density data from the ICI-3 sounding rocket and the GPS scintillation data, which gives us an opportunity to study plasma irregularities using two different observational techniques and investigate the relation between the cause (ionospheric irregularities) and the scintillation effect on the ground.

## 2. Instrumentation

The data set used in this study includes the measurements from the ESR at Longyearbyen, fitted flow vectors from the SuperDARN, GPS scintillation and total electron content (TEC) data from a receiver at Hornsund, and in situ measurements with the ICI-3 sounding rocket. The spatial coverage of these data sets is summarized in Figure 1.

The ESR at Longyearbyen consists of a 32-m steerable antenna and a 42-m static field-aligned antenna (azimuth = 184°, elevation = 82°). Both antennas allow for measurements of the electron density (Ne), electron temperature (Te), ion temperature (Ti), and line-of-sight ion velocity (Vi) as a function of range (e.g., Wannberg et al., 1997). The ESR was operated in a fast azimuth scan mode (Carlson et al., 2002) from 6:30 to 8:30 UT on 3 December 2011. The 32-m antenna beam moved between azimuth angles of 180° and 300° at an elevation angle of 30° and was alternating between clockwise and anticlockwise motion. The azimuthal scan speed of 0.625°/s allowed the radar beam to complete one 120°-wide azimuthal scan in 192 s. The selected pulse code experiment was *taro*, which utilizes both antennas for simultaneous transmission. The data were recorded every 6.4 s, which results in 30 adjacent radar beam directions in one complete azimuthal scan. In the current study, only data from the 32-m antenna is used. For data from the ESR 42 m, readers are referred to Jin et al. (2017). Figure 1 displays an example of one azimuthal scan at 7:27.23–7:30.35 UT when the RFE was observed. The field-of-view of the ESR 32-m antenna extended from 9 to around 10 magnetic local time and from 70° to 80° magnetic latitude.

The ICI-3 sounding rocket was launched from Ny-Ålesund (78.9°N, 11.9°E, geographic coordinates; 76.4°N, 110.2°E Corrected Geomagnetic Coordinates coordinates) at 07:21.31 UT on 3 December 2011. It reached an apogee of 354.5 km at 312.9 s after launch. The payload instruments included a low energy particle spectrometer (LEP), AC and DC electric field, and nine Langmuir probes. Five of the nine Langmuir probes were cylindrical "needle" Langmuir probes (the so-called multineedle Langmuir probe (m-NLP) system) which sampled at 8,680.5 Hz (Bekkeng et al., 2010; Jacobsen et al., 2010). In this study, we use probes 2, 4, and 5 to derive the electron density (see Figure 1 in Spicher et al., 2016). The LEP measures electron precipitation in the energy range of [0.01–7.9] keV (Saito et al., 2017). We use electron data at pitch angles of 0°–30° as a representative for precipitating electrons. For more details about the payload, see Spicher et al. (2016). In this study, we use the LEP data, the DC electric field data and the electron density data derived from the m-NLP system.

The GPS scintillation receiver is operated by the Space Research Center of the Polish Academy of Sciences at the Stanisław Siedlecki Polish Polar Station at Hornsund (Southern Spitsbergen, 77°N, 15.55°E; Corrected Geomagnetic Coordinates latitude: 74.11°N; Wernik et al., 2008). The receiver can provide TEC from the dual frequency measurements of the GPS signals. The 60-s amplitude ($S_4$) and phase scintillation indices ($\sigma_\phi$) are also recorded based on 50-Hz measurements of the amplitude and carrier phase at the GPS L1 frequency (1.57542 GHz; Van Dierendonck et al., 1993). In addition, the 50-Hz raw data of the amplitude and carrier phase at the GPS L1 frequency were used for calculating high-resolution (1 s) scintillation indices and
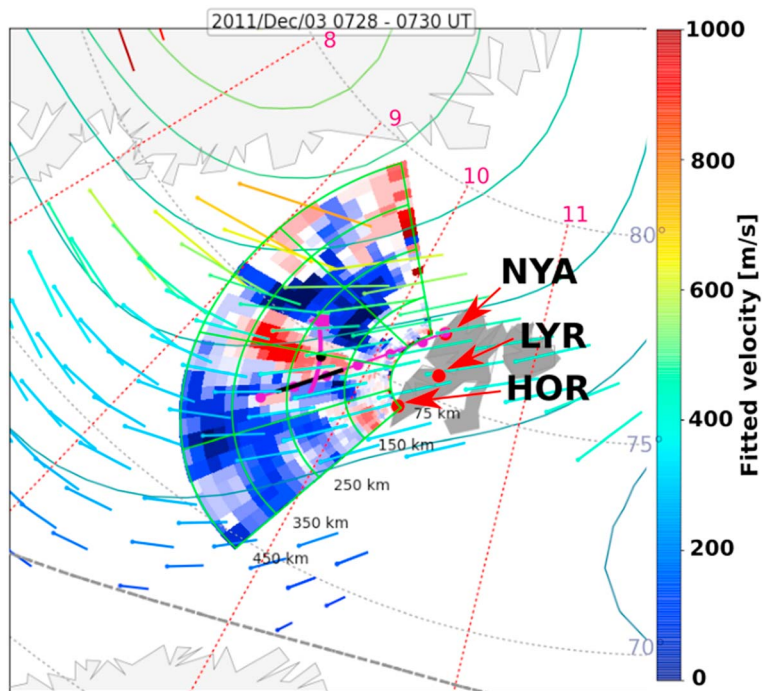
**Figure 1.** Overview of the instrumentation used in this study. The map is displayed in a magnetic latitude-magnetic local time coordinate system. The locations of Ny-Ålesund, Longyearbyen, and Hornsund are shown by red dots. The EISCAT Svalbard radar 32-m beam at Longyearbyen was operated in an azimuthal scan mode for azimuth angles of 180°–300° and at 30° elevation angle. The line-of-sight ion velocity data from the EISCAT Svalbard radar 32 m for 7:27.23–7:30.35 UT are plotted in the fan-shaped region, where red means flow away from the radar, and blue means flow toward the radar. The reversed flow event is the red region of flow away from the radar. The altitude of the radar measurements is indicated at 75, 150, 250, 350, and 450 km. The Investigation of Cusp Irregularities 3 sounding rocket was launched from Ny-Ålesund at 7:21.31 UT to intersect the reversed flow event. The Investigation of Cusp Irregularities 3 trajectory is shown by a magenta line and dots at 100-s cadence after the launch time. GPS satellite PRN30 was tracked from Hornsund, and its signal path intersected the reversed flow event. The ionospheric pierce points of PRN30 between 7 (magenta triangle) and 8 UT are shown by the pink line. The fitted drift velocities and electric potential contours from Super Dual Auroral Radar Network are overlayed to indicate the large-scale twin-cell convection pattern. The fitted Super Dual Auroral Radar Network velocities are color-coded according to the color bar on the right. NYA = Ny-Ålesund; LYR = Longyearbyen; HOR = Hornsund.

power spectra in this study (Jin & Oksavik, 2018). To calculate the amplitude and phase scintillation indices, we detrend the raw amplitude and carrier phase data using a cutoff frequency of 0.2 Hz (Jin & Oksavik, 2018).

To identify the large-scale convection patterns corresponding to the ESR data coverage, we also use observations from SuperDARN. The SuperDARN data were retrieved from Virginia Tech using the DaViTpy software package. SuperDARN convection patterns were created using data from all available radars and the technique of Ruohoniemi and Baker (1998), which generates the flow pattern every two minutes based on a fit of the ionospheric electrostatic potential in spherical harmonics.

The solar wind data and auroral electrojet (AE) indices from the OMNI database are used to present the upstream solar wind conditions and the Earth's magnetic response at high latitudes. The OMNI interplanetary magnetic field (IMF) is presented in the geocentric solar magnetospheric coordinates, and the solar wind data have been shifted from the observation points to the Earth's bow shock (King & Papitashvili, 2005).

## 3. Observations

In order to set the background for the in situ studies of plasma structures within the RFE with the ICI-3 rocket, we analyze the ionospheric conditions within a larger time period including the rocket launch.
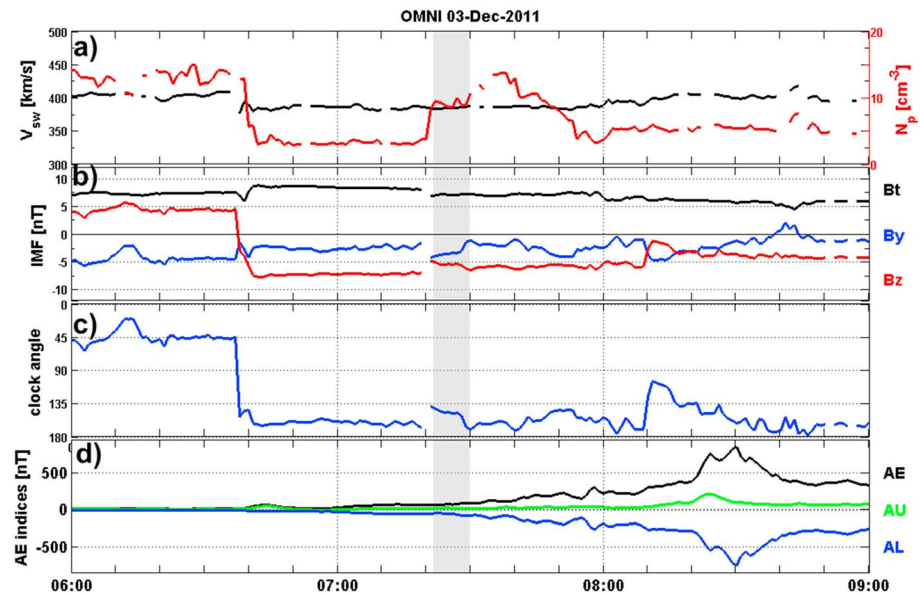
**Figure 2.** An overview of the solar wind and IMF parameters from the OMNI data set from 6:00 to 9:00 UT on 3 December, 2011. The launch window of Investigation of Cusp Irregularities 3 sounding rocket is indicated by grey shading. (a) The solar wind velocity (black) and proton density (Np, red). (b) The IMF strength (Bt, black), *By* (blue), and *Bz* (red) components. (c) The IMF clock angle. (d) AU (green), AL (blue), and AE (black) indices. IMF = interplanetary magnetic field.

We start with the solar wind and IMF data, which are presented in Figures 2a–2c for the period 6:00–9:00 UT. In the figure, the rocket launch window is gray shaded. While the solar wind velocity (black) was very stable around 400 km/s during the whole period, the proton density (Np, red) was dynamic and showed a steep decrease from 13 to 3 cm$^{-3}$ at 6:39 to 6:42 UT, followed by a steep increase from 4 to 9 cm$^{-3}$ at 7:20 to 7:22 UT. Note that such rapid changes in the solar wind could trigger the travelling convection vortices in the ionosphere (e.g., Friis-Christensen et al., 1988; Kim et al., 2017). However, that is outside the scope of the current paper, which focuses on the plasma irregularities associated with the RFE.

The IMF *By* was negative throughout the period of interest, and the strength decreased gradually. The IMF *Bz* was positive before 6:37 UT and turned southward for the next 2 hr, being strongly southward until 8:09 UT. This can also be clearly seen from the IMF clock angle (>135°) in Figure 2c. The clock angle ($\theta$) is defined as the angle between the *Z* axis and the projection of the IMF vector onto the geocentric solar magnetospheric *Y-Z* plane $\left(\theta = \mathrm{atan}\left(\frac{By}{Bz}\right)\right)$, resulting in values in the range $0° \leq \theta \leq 180°$. The AE indices are shown in Figure 2d. They provide a measure of the geomagnetic disturbance due to the auroral electrojets (Kamide & Rostoker, 2004). The AE indices were low before ~8:00 UT, and they increased gradually afterward. One substorm occurred around 8:30 UT, as shown by the rapid decrease of the AL index to −747 nT. The gray shaded region in all panels corresponds to the ICI-3 rocket flight and the observation of the RFE. This time interval was characterized by a steady solar wind velocity, a sudden increase of the density (and the solar wind dynamic pressure - not shown), a strongly negative IMF *Bz* and weakly negative *By*, and generally low geomagnetic disturbance.

Within the context of the solar wind and IMF parameters, now we focus on the time when the RFE was observed, that is, between 7:15 and 7:40 UT. Figure 3 shows the line-of-sight ion velocity (Vi) from six consecutive sweeps of the ESR 32-m antenna. The map potential model output from the SuperDARN network is overlaid with thick black contour lines to indicate the large-scale convection pattern. In order to assist the discussion, the ESR field-of-view is subdivided in four wedge sectors increasing clockwise from 1 to 4 and four regions i–iv with increasing radial distance. This subdivision is annotated in Figure 3a.

In Figure 3a, we see a strong eastward flow channel with magnitude larger than 1 km/s (dark blue) mainly in sector 3 and partly in sectors 2 and 4. The flow channel was divided in two by a narrow area of slightly
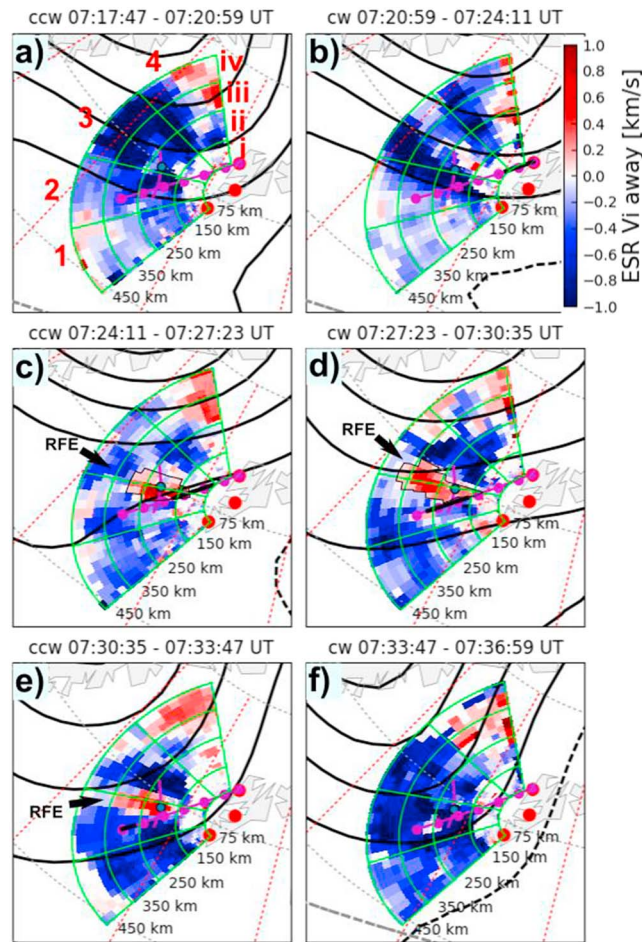
**Figure 3.** Line-of-sight ion velocity ($V_i$) from the ESR 32-m dish. Positive (red) velocities are away from the radar. The convection pattern from SuperDARN is overlayed by thick black contour lines. The RFE that is flowing away from the radar (red color) is annotated by black arrow in panels (c)–(e). The scan time is shown on the top of each panel, where "cw" means clockwise and "ccw" means counterclockwise. The GPS pierce points and the Investigation of Cusp Irregularities 3 trajectory are shown in magenta segments. See text for more details. The thin black contours around the RFE in (c) and (d) are used to assist the comparison with Figure 4. ESR = EISCAT Svalbard radar; RFE = reversed flow event.

westward flow (white to red) in Figure 3b. In Figure 3c, the RFE was formed between sectors 2 and 3 (slightly south of 75° magnetic latitude). The RFE is well defined in Figures 3c–3e between 7:24.11 and 7:33.47 UT. The westward RFE was bounded by eastward plasma flow on the equatorward and poleward sides. Figure 3f shows that the RFE disappeared abruptly after 07:33 UT. The RFE was observed in four ESR scans (i.e., a total duration of ~13 min), with the reversed flow velocity up to 0.5 km/s which was bounded on both sides by the eastward flow up to more than 1 km/s. The largest velocity shear was observed between the radar beams in sector 3, where the ion velocity changed from −0.5 to 1.2 km/s. The estimated velocity gradient was $\Delta V/L = (1.7\ km/s)/(91\ km) = 0.0187 s^{-1}$. The RFE was almost stationary in latitude during its lifetime. This is different from previous studies by Oksavik et al. (2004) and Oksavik et al. (2005) where an RFE was observed to move poleward in tandem with a PMAF. However, Moen et al. (2008) also observed one RFE that stayed along with a bright background arc that did not move poleward.

For a complete information, we also show the other three parameters from the ESR 32 m data: the electron density (Ne), electron temperature (Te), and ion temperature (Ti). Figure 4 shows these parameters for two ESR scans that were coincident in time with the ICI-3 crossing of the RFE (i.e., corresponding to Figures 3c–3d). To assist the comparison between the figures, we superimpose the shape of the RFE in each panel. Since the radar beam was scanning at an elevation angle of 30°, the observations do not only show the horizontal
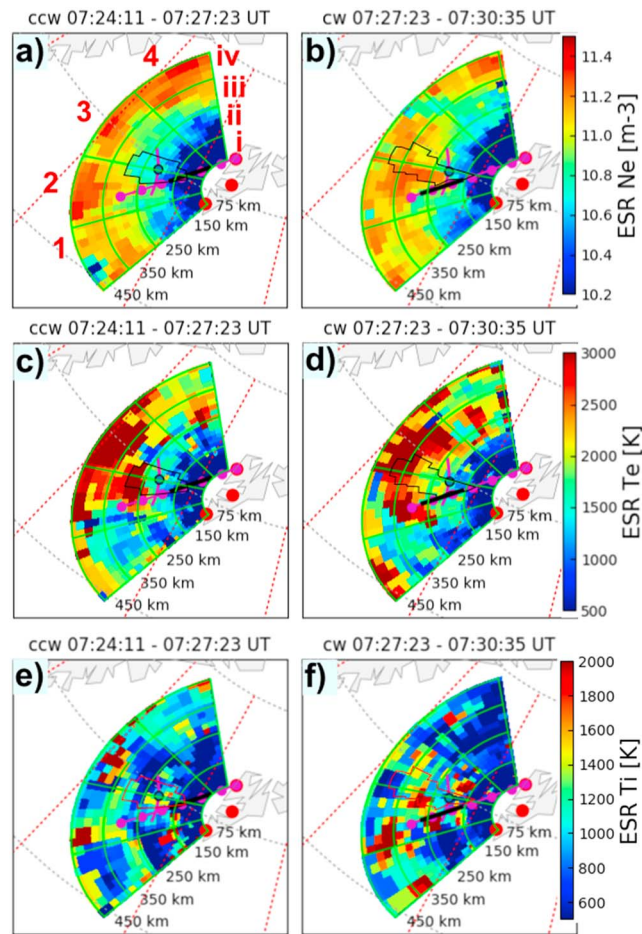
**Figure 4.** The electron density (a–b), electron temperature (c–d), and ion temperature (e–f) from the ESR 32 m during two azimuth scans during the same time periods as Figure 3c–3d, that is, when the ICI-3 crossed the RFE area. The shape of the RFE is drawn in black and magenta polygons in panels a–d and e–f, respectively. The shape is derived from Figures 3c to 3d. ESR = EISCAT Svalbard radar.

variations but also the variations as a function of altitude. The altitudes of each subsector are annotated at the bottom of the fan in each panel.

Figure 4a shows that Ne was highest in region iv, that is, above 350 km. This is most likely due to the altitude profile of the ionospheric *F* region density that peaked around 350 km. However, the enhanced Ne was also observable equatorward of the RFE at lower altitudes. Figure 4b indicates that Ne was enhanced both equatorward and poleward of the RFE. The enhanced Ne was visible down to 150-km altitude on the equatorward boundary of the RFE. These enhancements were likely due to cusp type soft particle precipitation (Moen, van Eyken, & Carlson, 2001).

Figures 4c–4f show the corresponding measurements of Te and Ti. Enhanced Te is often observed in the cusp region as a result of soft electron precipitation (Doe et al., 2001; Lockwood et al., 1993; Moen et al., 2004). The enhanced Te was mostly above the altitude of 250 km, even though some enhancement near the RFE at lower altitude is also visible. Enhanced Te can be observed during ongoing electron precipitation and when the ambient ionospheric density is low. The cooling rate due to coupling with ions and neutrals is proportional to the square of the electron density. Therefore, a bite-out in Te is seen when Ne is larger than $2 \times 10^{11}$ m$^{-3}$ (Carlson, 1998; Moen et al., 2004).

Ti can be enhanced in the ionosphere due to the ion frictional heating when the ion velocity is large enough relative to the neutrals (Carlson et al., 2012; Ogawa et al., 2001; Rodger et al., 1994; Skjaeveland et al., 2017; Valladares et al., 1994). The enhanced Ti started to appear near the equatorward boundary of the RFE in
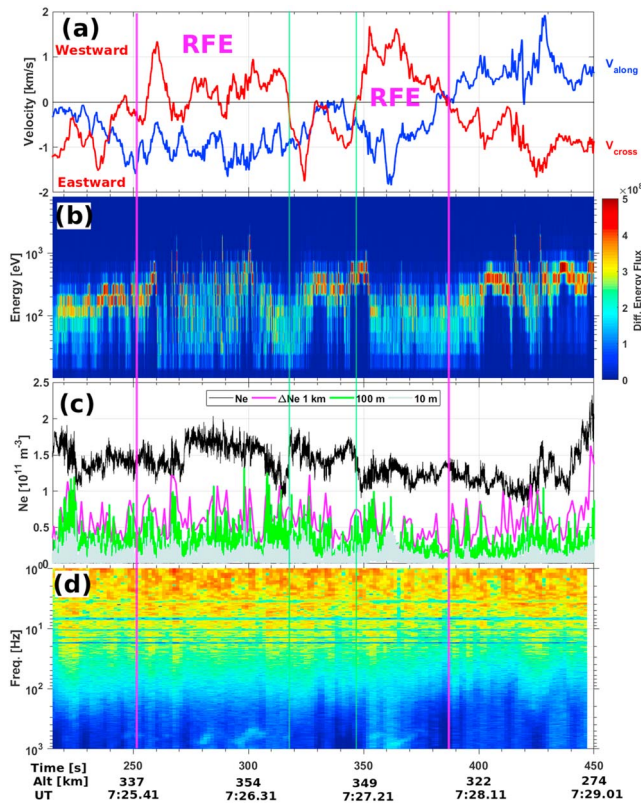
**Figure 5.** Observations from the Investigation of Cusp Irregularities 3 sounding rocket. The time is seconds after launch (7:21.31 UT). The corresponding UT and rocket altitude are also indicated below the figure. (a) The along-track and cross-track velocities relative to the rocket trajectory. (b) The precipitating electron flux. (c) The absolute electron density (Ne) from the m-NLP system in black and corresponding electron density fluctuations (ΔNe) in different colors at 1 km, 100 m, and 10 m. Ne is in the unit of $10^{11}$ $m^{-3}$, while ΔNe is in the unit of $10^{10}$ $m^{-3}$. (d) A spectrogram of the electron density fluctuations. RFE = reversed flow event.

Figure 4e. The enhanced Ti became stronger and clearer in Figure 4f. We are aware that the ion temperature measurements were very noisy and perhaps the scan period 192 s for the ESR is not able to resolve the rapid spatiotemporal variation of Ti. However, from the ESR data, we show that both the GPS pierce point and ICI-3 were in a region of enhanced Ti.

After presenting the background plasma conditions monitored by the ESR and SuperDARN, we now proceed with presenting the in situ data from the ICI-3 sounding rocket. The full path of ICI-3 is shown by a magenta line in each panel of Figure 3, with magenta dots in 100-s cadence after the launch time. The ICI-3 trajectory during each ESR scan time is highlighted in black in Figures 3b–3e. ICI-3 intersected the RFE region roughly between 250 and 400 s after launch, as it is also indicated in Figures 3c and 3d. The high-resolution in situ measurements allow for the detection of fine-scale structures within the RFE.

Figure 5a shows the along-track (blue) and cross-track (red) components of the horizontal velocity with respect to the rocket trajectory. The cross-track velocity ($V_{cross}$) is mainly in the E-W direction, whilst the along-track velocity ($V_{along}$) translates to the N-S component. Consistent with Figure 3, the ICI-3 traverse of the RFE region is seen in the cross-track velocity shown in Figure 5a, where $V_{cross}$ shows an interval of westward flow (reversed flow) at 255–380 s, which was bounded by eastward flow. Note that there was a short interval of the eastward flow at 318–346 s (inside the RFE). This was not observed by the ESR due to its spatial resolution as it could only provide the mesoscale information of the RFE embedded in the large-scale convection pattern. The in situ rocket measurements account for even smaller structures within the RFE and suggests that the RFE can include fine-scale flow structures.

The precipitating electron data is shown in Figure 5b, which was measured by the LEP instrument onboard the ICI-3 rocket. Inverted-V structures were observed at 220–260, 326–352, and after 400 s. These inverted Vs were likely associated with upward field aligned currents (Moen et al., 2008). There were also two intervals of broadband electron precipitation: between 260 and 326 s and 353 and 400 s. These two intervals were likely associated with the downward field-aligned Birkeland currents.

The in situ electron density (Ne) data is shown in Figure 5c in black. There were no strong large-scale density gradients as those usually observed in polar cap patches (e.g., Moen et al., 2012; Spicher et al., 2014). The weak but visible large-scale density enhancements (in time intervals of 280–315 and 320–340 s) may be linked to the corresponding particle precipitation. However, the link between a local particle impact ionization and electron density enhancements is not direct above 200 km where the characteristic time for recombination is several minutes (Lockwood & Carlson, 1994; Rodger et al., 1994; Skjaeveland et al., 2017). The measured plasma can also be transported from elsewhere (e.g., Kelley et al., 1982; Oksavik et al., 2010). Though there were no clear steep density gradients, the electron density was significantly fluctuated. To present the density variations, we derive the electron density fluctuations (ΔNe) at different scales (1 km and 100 m and 10 m) in Figure 5c. The density fluctuations are derived by calculating the RMS of the detrended Ne at certain window (1 km and 100 m and 10 m), where Ne is detrended by removing its moving average values. For example, $Ne' = Ne - Ne\_sm$, where Ne is the original electron density, $Ne\_sm$ is the smoothed electron density by a moving average at certain window, and $Ne'$ is the detrended electron density. Note that in Figure 5c, Ne is in unit of $10^{11}$ $m^{-3}$, while ΔNe is in the unit of $10^{10}$ $m^{-3}$. The electron density fluctuations at 1 km were present throughout the whole flight, and they were independent of the particle precipitation and the plasma flow direction. The largest fluctuations (i.e., >1 × $10^{10}$ $m^{-3}$ or 1% of the absolute electron density) were present both inside and outside of the RFE and were independent of the flow reversal. This
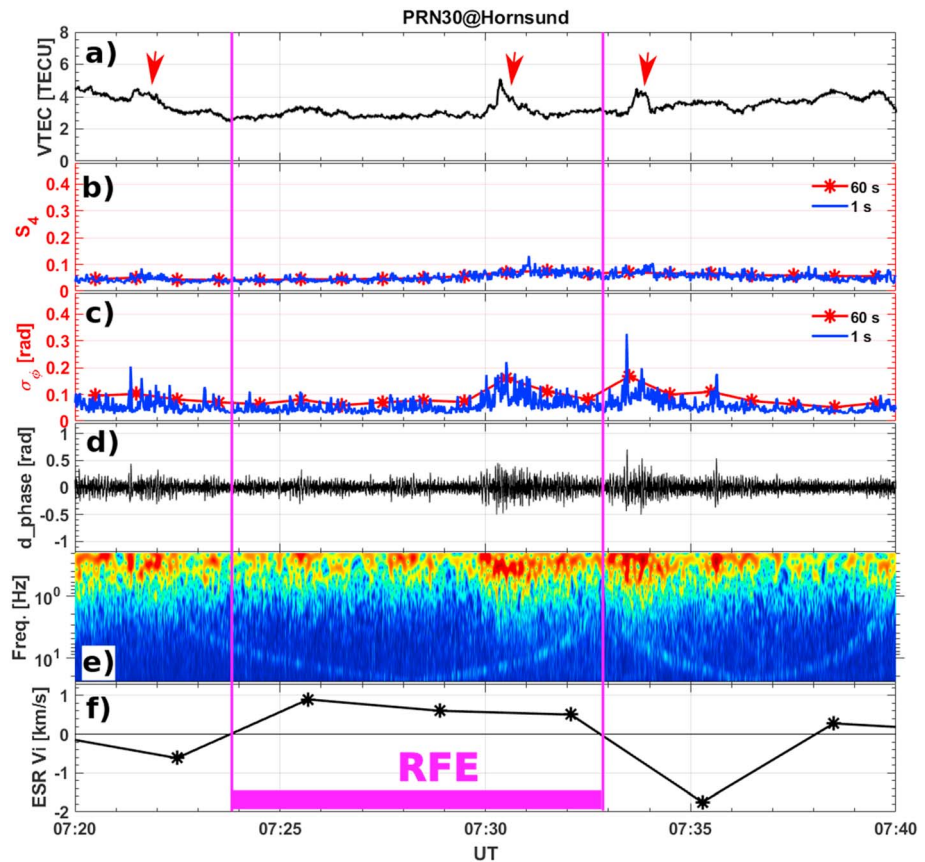
**Figure 6.** The GPS PRN30 data observed from Hornsund. (a) The VTEC. (b) The 60-(red) and 1-s (blue) amplitude scintillation indices (S$_4$). (c) The 60- (red) and 1-s (blue) phase scintillation indices ($\sigma_\phi$). (d) The detrended carrier phase (d_phase) with a sixth order high-pass Butterworth filter at a cutoff frequency of 0.2 Hz. (e) A spectrogram of the carrier phase. (f) The line-of-sight velocity data near the pierce point of PRN30 as extracted from the ESR data. ESR = EISCAT Svalbard radar; RFE = reversed flow event; VTEC = vertical total electron content.

is the main characteristics of the KHI, which can develop irregularities independent of the direction of flow shears and density gradients. The density fluctuations at 100 m and 10 m show similar characteristics as those at the 1-km scale.

To present the electron density fluctuations at different scales, we show in Figure 5d a spectrogram of the electron density as a function of time (UT) and frequency (Hz) (Spicher et al., 2016). The spectrogram is generated using the MATLAB built-in function *spectrogram*, where the spectrogram presents the Fourier transform of the relative density fluctuations using a Hamming window of 6-s intervals. The power spectral density (PSD) shows a broadband feature indicative of irregularities over a broad range of scales (from 1 to above 100 Hz). The PSD is relatively homogeneous over the whole flight, with several pulses of enhanced power corresponding to peaks in the 1-km density fluctuations (see Figure 5c). The interval at 350–365 s shows enhanced PSD down to 10$^3$ Hz (corresponding to a 1-m spatial scale) and was studied in detail by Spicher et al. (2016).

The plasma irregularities could also be studied with the ground-based GPS scintillation receiver. The GPS pierce points of PRN30 tracked from Hornsund intersected the RFE. Figure 3 shows the pierce points from 7:00 to 8:00 UT as a North-South (N-S) aligned magenta segment. PRN30 was at an elevation angle of ~50° during the time of interest. By assuming the ionosphere to be at 350-km altitude, the GPS pierce point moved southward at the speed of ~66 m/s. The location of the pierce point during the corresponding ESR scan time is shown by a green dot in Figure 3. The GPS data from PRN30 at 7:20–7:40 UT are displayed in Figures 6a–6e. In addition, Figure 6f shows the ion velocity data that are extracted from the ESR 32-m antenna in the vicinity of the pierce point of PRN30. The velocity data have the same resolution as the
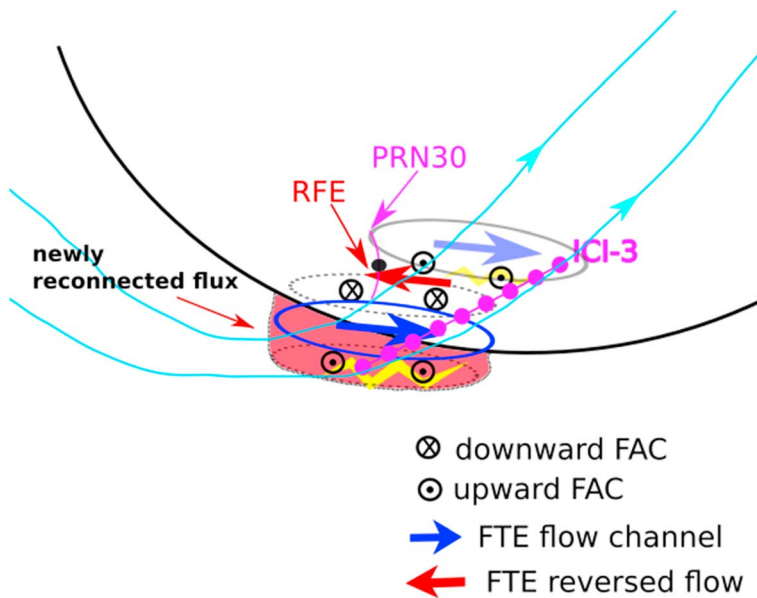
**Figure 7.** A sketch of the observation geometry. The newly reconnected magnetic flux is presented by the red bulge. The blue ellipse and arrow present the flow channel associated with the newly reconnected flux. The return flow on the poleward side is the RFE. The circled dots and crosses represent the upward and downward field-aligned currents. The gray ellipse is the previously reconnected flux that has been transported poleward into the polar cap. See text for more details. ICI-3 = Investigation of Cusp Irregularities 3; FTE = flux transfer event; RFE = reversed flow event.

ESR scan (i.e., 192 s). The positive ion velocity (away from the ESR) is the RFE as identified in Figure 3, and it is delimited by two vertical magenta lines in Figure 6.

Figure 6a shows that the vertical TEC and consequently the electron density gradually decreased as there was no high-density plasma transported into this region from the prenoon convection cell during the time of interest (see Jin et al., 2017). Besides the decreasing vertical TEC, there were three increases in TEC indicative of local ionizations from particle precipitation. These are annotated by red arrows in Figure 6a.

Figures 6b–6c show the GPS amplitude scintillation ($S_4$) and phase scintillation indices ($\sigma_\phi$) with 1-(blue) and 60-s (red) resolution. These indices were calculated by detrending the raw (50 Hz) data with a cutoff frequency of 0.2 Hz. Note that the amplitude scintillation is caused only by the diffractive effect, while the phase scintillation can be caused by both refractive and diffractive effects (De Franceschi et al., 2019; McCaffrey & Jayachandran, 2019; Wang et al., 2018). $\sigma_\phi$ is sensitive to the cutoff frequency when detrending the raw carrier phase (Forte & Radicella, 2002). We tested different cutoff frequencies. The result for the traditional cutoff frequency of 0.1 Hz is presented in the supporting information (SI), where $\sigma_\phi$ shows similar features as in Figure 6.

The GPS amplitude scintillations were generally quiet throughout the time of interest. $S_4$ was well below 0.1, except for a short time period after 7:30 UT when $S_4$ reached slightly above 0.1. This was possibly related to a simultaneous small TEC enhancement by particle precipitation. Contrary to the quiet amplitude scintillations, the GPS phase scintillations ($\sigma_\phi$) were moderate and variable (Figure 6c). The three TEC pulses annotated in Figure 6a were all associated with enhanced GPS phase scintillations. This is mostly clear in the high-resolution (1s) $\sigma_\phi$ data. $\sigma_\phi$ was low and stable at 7:23–7:30 UT, when the pierce point of PRN30 was within the RFE. However, during the late phase of the RFE, the GPS phase scintillations enhanced abruptly. $\sigma_\phi$ increased from the noise level (0.05 rad) to 0.2 rad at 7:30 UT coinciding with the enhanced TEC. From Figure 3, we see that the RFE emerged in Figure 3c (7:24 UT) and it grew in east-west direction in Figures 3d–3e, after which it suddenly disappeared in Figure 3f (7:33 UT). During its lifetime, the RFE barely moved in the latitudinal direction. Therefore, PRN30 did not cross the whole latitudinal range of the RFE. Rather, it was located near the center of the RFE around 7:24–7:27 UT, and it was located near the poleward edge of the RFE around 7:30 UT (cf. Figure 3d). It was around 7:30 UT that PRN30 experienced an increase in TEC and enhanced scintillation level. This is consistent with Figure 7 in section 4.

Figure 6d shows the detrended GPS carrier phase based on the 50-Hz raw data. The carrier phase measurement was detrended by first subtracting a fourth-order polynomial fit from the raw phase and then filtering the remainder using a high-pass Butterworth filter with a cutoff frequency of 0.2 Hz (van der Meeren et al., 2014). The one using 0.1 Hz can be found in the SI. The detrended data show similar signatures to the 1-s resolution $\sigma_\phi$, that is, clear responses to the pulsed TEC enhancements. The spectrogram of the GPS carrier phase provides more complete information about the GPS carrier phase fluctuations. Figure 6e displays a wavelet spectrogram as a function of frequency (Hz) and UT (Torrence & Compo, 1998). The spectrogram indicates that the phase varied over a wide range of frequency when $\sigma_\phi$ was enhanced near 7:30 and 7:33 UT. The enhanced power went down to nearly 10 Hz around 7:30 UT. The increases in the PSD of the carrier phase data indicate the existence of enhanced electron density fluctuations at a similar spatial scale. This will be discussed in section 4.

## 4. Discussion

In this study, we have used multiple techniques to probe one RFE, that is, the ESR, the ICI-3 sounding rocket, and GPS data. The RFE developed gradually and remained relatively stationary in latitude for three consecutive ESR scans before it suddenly disappeared. The lifetime of the RFE was about 13 min. The velocity of the RFE was +0.5 km/s as compared to the background velocity of −1 km/s of the surrounding flow. The high-resolution in situ electric field measurement from ICI-3 shows that the RFE velocity reached 1.5 km/s, with complex substructures of alternating plasma flows in the eastward and westward directions.

Since we do not have in situ magnetic field data from the ICI-3, which can derive the field-aligned currents, nor ground-based optical auroral measurements, which can monitor the exact location of auroral arcs, we can only infer the observational geometry from the other data sets that we have presented and previous literature (Moen et al., 2008; Rinne et al., 2007). Rinne et al. (2007) proposed an asymmetric Southwood (1987) FTE model where the RFE is the return flow on the poleward side of the newly reconnected magnetic flux. We thus summarize our measurements in Figure 7 within the framework of Rinne et al. (2007). In Figure 7, the red bulge represents the newly reconnected flux tube. The blue thick arrow and ellipse represent the eastward flow channel due to the magnetic tension force, which is consistent with the negative IMF *By*. The RFE in this study is the return flow of the newly reconnected flux, which is located poleward of the center flux (indicated by a dotted grey ellipse). The ESR 32-m data confirm that there was a region of eastward flow poleward of the RFE (cf. Figure 3d). This was probably the reminiscent of a previously opened flux tube that has already been transported into the polar cap. This "old" opened flux is represented by the solid gray ellipse and the light blue arrow of eastward flow. The circled dots and crosses represent the upward and downward FAC system, according to the Southwood (1987) FTE model. There is an upward FAC on the equatorward side of the FTE flow channel and a downward FAC on the poleward side. Moen et al. (2008) showed that a thin Birkeland current arc is always located at the sharp clockwise flow reversal, consistent with a converging electric field and an upward FAC. The upward FAC on the equatorward side of the FTE center flux should correspond to an auroral arc that is presented in yellow. The upward FAC on both sides of the RFE was consistent with the particle measurements from the LEP instrument onboard ICI-3 (cf. Figure 5), which showed inverted Vs before and after the RFE region.

In Figure 7, the magenta line with dots represents the ICI-3 trajectory that intersected the RFE, and the thin magenta segment with a black dot to the west (left) represents the pierce point of GPS PRN30 that also intersected the RFE at the same time. Both the in situ electron density data and the ground-based GPS scintillation data show plasma density irregularities associated with the RFE. One way to connect the in situ electron density measurement and the ground-based scintillation data is to compare their power spectral slopes (e.g., Basu et al., 1988; Kelley et al., 1980). Since, the scintillations on the ground are due to the scattering of the GPS signals by the ionospheric irregularities and the interference when the radio waves propagate away from the irregular phase screen (Rino, 1979).

Figures 8a–8b show two examples of power spectra of the detrended GPS carrier phase (note that the cutoff frequency is 0.1 Hz to extend the valid frequency range). The spectra show a power-law spectrum, and the black lines show linear fits to the spectral slopes. The spectral slopes $p$, which were fitted in the frequency range 0.2–2 Hz, are shown in the top right corner of each panel. The spectral slopes were −2.61 and −2.57, respectively. These slopes are consistent with the result in Jin and Oksavik (2018). Figure 8c shows
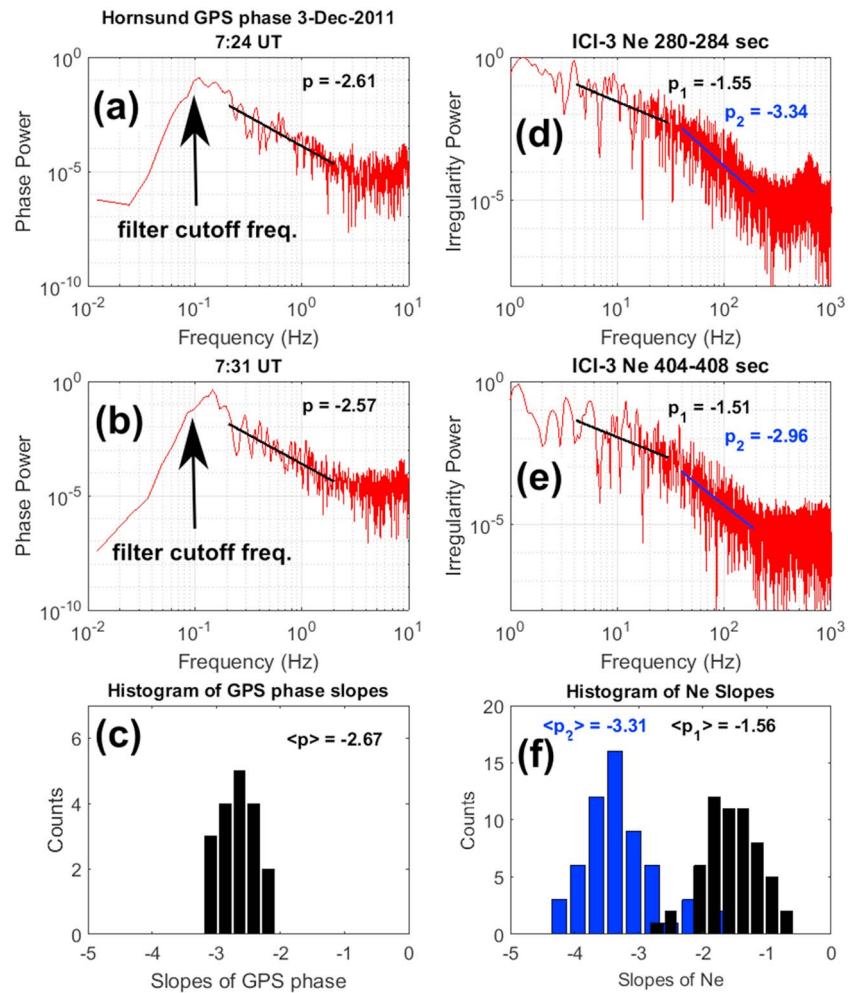
**Figure 8.** Power spectra and fitted slopes for (a–b) the detrended GPS carrier phase and (d–e) the electron density from ICI-3. In (a–b), the spectral slopes are linearly fitted from 0.2 to 2 Hz. The fits are shown in black, and the power law index is shown on the top right of each panel. (c) The histogram of the spectral slopes of the GPS phase measurements at 7:20–7:37 UT, where the average slope is shown on the top right. In (d–e), the spectral slopes are linearly fitted in two separate intervals; low frequency (4–30 Hz) and high frequency (40–190 Hz). The low- and high-frequency fits with slopes are shown in black and blue, respectively. (f) A histogram of the ICI-3 rocket electron density spectral slopes, where the low frequency slopes are shown in black, and the high frequency slopes are shown in blue. Average values for the slopes are shown on the top. ICI-3 = Investigation of Cusp Irregularities 3.

the distribution (histogram) of the spectral slopes from 7:20 to 7:37 UT. The slopes varied from −2 to −3, with an average of −2.67.

Similar to the scintillation data, we show two examples in Figures 8d–8e for the power spectra of the detrended electron density data. If we assume that the RFE was stationary in magnetic latitude during its lifetime, which was the situation for the current event, we can convert the data from a temporal scale to a spatial scale. The pierce point of GPS PRN30 moved southward at a speed of ~66 m/s. The frequency range of 0.2–2 Hz in the GPS data corresponds to 330–33 m in a spatial scale. By using 1 km/s (the speed of the ICI-3 rocket), this spatial scale corresponds to a frequency range of 3–30 Hz in the low frequency part of the ICI-3 electron density power spectra. The black lines of Figures 8d–8e are linear fits to the low frequency part of the power spectra. Spicher et al. (2014) reported that the electron density at high latitudes often shows double-slope power spectra. For completeness, we therefore also show linear fits to the high frequency part (40–190 Hz) of the ICI-3 electron density power spectra. The histogram of the spectral slopes in the low and high frequency parts are presented in Figure 8f in black and blue colors, respectively. This result is similar to

Figure 3 of Spicher et al. (2014). However, Spicher et al. (2014) presented the spectral slopes of the electron density data in 2-s intervals, while we use 4-s intervals. Still it does not affect the general features such as the double slope of the electron density power spectra.

The low-frequency part of the electron density fluctuation should correspond to the GPS phase scintillation data. In the scenario of weak scattering (Rino, 1979), which was the case for the current study, the phase screen theory predicts that the spectral slope of the in situ electron density data should be bigger by 1 compared to the slope of the corresponding phase scintillation data (Basu et al., 1988; Cronyn, 1970). With this in mind, the result of the scintillation data and the in situ data match quite well, that is, the average slope of the phase scintillation data was −2.67 which was about 1 less than the average slope of the low frequency fluctuations of the electron density data (−1.56). The GPS carrier phase measurement from the NovAtel GPS scintillation receiver is noisy above 10 Hz (Van Dierendonck et al., 1993). Therefore, the GPS phase data cannot reflect the high frequency fluctuations of the electron density data. The GPS phase power spectra only show a single slope instead of the double slope. If it was possible to measure higher frequency GPS phase variations, the slope of high frequency part of the GPS phase scintillations should be on the order of −4.3 ($<p_2>$−1) according to the phase scintillation theory.

## 5. Summary and Conclusion

In this paper, we have presented an overview of the ionospheric conditions during the launch of the ICI-3 sounding rocket. The ESR 32-m data show a clear RFE with velocity of +0.5 km/s as opposed to the background flow of −1 km/s. The RFE lasted for ~13 min. ICI-3 detected reversed flow (up to 1.5 km/s) and more complex substructures within the RFE. The high-resolution in situ electron density data show broadband plasma irregularities down to meter scales. The GPS scintillation data from the Hornsund station revealed that the pierce point of GPS PRN30 was located inside the RFE when ICI-3 intersected the RFE. It allowed us to directly compare the ground-based GPS scintillation data with in situ electron density irregularities inside the RFE. The GPS scintillation data show moderate phase scintillations and weak amplitude scintillations. A study of the power spectra of the in situ electron density data and the GPS carrier phase revealed that the spectral slope of the electron density data in the lower frequency range matches the ground-based GPS carrier phase measurements quite well. It suggests that it is now in principle possible to model the GPS scintillations from high-resolution in situ electron density data from individual sounding rockets or a fleet of CubeSat in low-Earth orbit.

## References

Basu, S., Basu, S., Weber, E. J., & Coley, W. R. (1988). Case-study of polar-cap scintillation modeling using De-2 irregularity measurements at 800 km. *Radio Science*, 23(4), 545–553. https://doi.org/10.1029/RS023i004p00545

Bekkeng, T. A., Jacobsen, K. S., Bekkeng, J. K., Pedersen, A., Lindem, T., Lebreton, J. P., & Moen, J. I. (2010). Design of a multi-needle Langmuir probe system. *Measurement Science and Technology*, 21(8). https://doi.org/10.1088/0957-0233/21/8/085903

Carlson, H. C. (1998). Response of the polar cap ionosphere to changes in (solar wind) IMF. In *Polar cap boundary phenomena* (pp. 255–270). Dordrecht: Springer.

Carlson, H. C. (2012). Sharpening our thinking about polar cap ionospheric patch morphology, research, and mitigation techniques. *Radio Science*, 47, RS0L21. https://doi.org/10.1029/2011RS004946

Carlson, H. C., Oksavik, K., Moen, J., van Eyken, A. P., & Guio, P. (2002). ESR mapping of polar-cap patches in the dark cusp. *Geophysical Research Letters*, 29(10), 1386. https://doi.org/10.1029/2001GL014087

Carlson, H. C., Pedersen, T., Basu, S., Keskinen, M., & Moen, J. (2007). Case for a new process, not mechanism, for cusp irregularity production. *Journal of Geophysical Research*, 112, A11304. https://doi.org/10.1029/2007JA012384

Carlson, H. C., Spain, T., Aruliah, A., Skjaeveland, A., & Moen, J. (2012). First-principles physics of cusp/polar cap thermospheric disturbances. *Geophysical Research Letters*, 39, L19103. https://doi.org/10.1029/2012GL053034

Cronyn, W. M. (1970). Analysis of Radio Scattering and Space-Probe Observations of Small-Scale Structure in Interplanetary Medium. *Astrophysical Journal*, 161(2), 755. https://doi.org/10.1086/150576

De Franceschi, G., Spogli, L., Alfonsi, L., Romano, V., Cesaroni, C., & Hunstad, I. (2019). The ionospheric irregularities climatology over Svalbard from solar cycle 23. *Scientific reports-UK*, 9(1). https://doi.org/10.1038/s41598-019-44829-5

Doe, R. A., Kelly, J. D., & Sanchez, E. R. (2001). Observations of persistent dayside F region electron temperature enhancements associated with soft magnetosheath like precipitation. *Journal of Geophysical Research*, 106(A3), 3615–3630. https://doi.org/10.1029/2000JA000186

Forte, B., & Radicella, S. M. (2002). Problems in data treatment for ionospheric scintillation measurements. *Radio Science*, 37(6), 1096. https://doi.org/10.1029/2001RS002508

Friis-Christensen, E., McHenry, M., Clauer, C., & Vennerstrøm, S. (1988). Ionospheric traveling convection vortices observed near the polar cleft: A triggered response to sudden changes in the solar wind. *Geophysical Research Letters*, 15(3), 253–256. https://doi.org/10.1029/GL015i003p00253

Jacobsen, K. S., Pedersen, A., Moen, J. I., & Bekkeng, T. A. (2010). A new Langmuir probe concept for rapid sampling of space plasma electron density. *Measurement Science and Technology*, 21(8). https://doi.org/10.1088/0957-0233/21/8/085902

Jin, Y., Moen, J. I., & Miloch, W. J. (2015). On the collocation of the cusp aurora and the GPS phase scintillation: A statistical study. *Journal of Geophysical Research: Space Physics*, *120*, 9176–9191. https://doi.org/10.1002/2015JA021449

Jin, Y. Q., Miloch, W. J., Moen, J. I., & Clausen, L. B. N. (2018). Solar cycle and seasonal variations of the GPS phase scintillation at high latitudes. *Journal of Space Weather and Space Climate*, *8*. https://doi.org/10.1051/swsc/2018034

Jin, Y. Q., Moen, J. I., Oksavik, K., Spicher, A., Clausen, L. B. N., & Miloch, W. J. (2017). GPS scintillations associated with cusp dynamics and polar cap patches. *Journal of Space Weather and Space Climate*, *7*. https://doi.org/10.1051/swsc/2017022

Jin, Y. Q., & Oksavik, K. (2018). GPS scintillations and losses of signal lock at high latitudes during the 2015 St. Patrick's Day storm. *Journal of Geophysical Research: Space Physics*, *123*, 7943–7957. https://doi.org/10.1029/2018JA025933

Kamide, Y., & Rostoker, G. (2004). What is the physical meaning of the AE index?, *Eos. Transactions of the American Geophysical Union*, *85*(19), 188–192. https://doi.org/10.1029/2004EO190010

Kelley, M. C., Baker, K. D., Ulwick, J. C., Rino, C. L., & Baron, M. J. (1980). Simultaneous rocket probe, scintillation, and incoherent-scatter radar observations of irregularities in the auroral-zone ionosphere. *Radio Science*, *15*(3), 491–505. https://doi.org/10.1029/RS015i003p00491

Kelley, M. C., Vickrey, J. F., Carlson, C. W., & Torbert, R. (1982). On the origin and spatial extent of high-latitude *F*-region irregularities. *Journal of Geophysical Research*, *87*(Na6), 4469–4475. https://doi.org/10.1029/JA087iA06p04469

Kim, H., Lessard, M. R., Jones, S. L., Lynch, K. A., Fernandes, P. A., Aruliah, A. L., et al. (2017). Simultaneous observations of traveling convection vortices: Ionosphere-thermosphere coupling. *Journal of Geophysical Research: Space Physics*, *122*, 4943–4959. https://doi.org/10.1002/2017JA023904

King, J. H., & Papitashvili, N. E. (2005). Solar wind spatial scales in and comparisons of hourly Wind and ACE plasma and magnetic field data. *Journal of Geophysical Research*, *110*, A02104. https://doi.org/10.1029/2004JA010649

Lockwood, M., & Carlson, H. C. (1994). Production of polar-cap electron-density patches by transient magnetopause reconnections–Reply. *Geophysical Research Letters*, *19*(17), 1731–1734. https://doi.org/10.1029/92GL01993

Lockwood, M., Denig, W., Farmer, A., Davda, V., Cowley, S., & Lühr, H. (1993). Ionospheric signatures of pulsed reconnection at the Earth's magnetopause. *Nature*, *361*(6411), 424–428. https://doi.org/10.1038/361424a0

McCaffrey, A. M., & Jayachandran, P. T. (2019). Determination of the refractive contribution to GPS phase "scintillation". *Journal of Geophysical Research: Space Physics*, *124*, 1454–1469. https://doi.org/10.1029/2018JA025759

Moen, J., Carlson, H. C., Milan, S. E., Shumilov, N., Lybekk, B., Sandholt, P. E., & Lester, M. (2001). On the collocation between dayside auroral activity and coherent HF radar backscatter. *Annales Geophysicae*, *18*(12), 1531–1549. https://doi.org/10.1007/s005850000302

Moen, J., Lockwood, M., Oksavik, K., Carlson, H. C., Denig, W. F., van Eyken, A. P., & McCrea, I. W. (2004). The dynamics and relationships of precipitation, temperature and convection boundaries in the dayside auroral ionosphere. *Annales Geophysicae - Germany*, *22*(6), 1973–1987. https://doi.org/10.5194/angeo-22-1973-2004

Moen, J., Oksavik, K., Abe, T., Lester, M., Saito, Y., Bekkeng, T. A., & Jacobsen, K. S. (2012). First in-situ measurements of HF radar echoing targets. *Geophysical Research Letters*, *39*, L07104. https://doi.org/10.1029/2012GL051407

Moen, J., Rinne, Y., Carlson, H. C., Oksavik, K., Fujii, R., & Opgenoorth, H. (2008). On the relationship between thin Birkeland current arcs and reversed flow channels in the winter cusp/cleft ionosphere. *Journal of Geophysical Research*, *113*, A09220. https://doi.org/10.1029/2008JA013061

Moen, J., van Eyken, A. P., & Carlson, H. C. (2001). EISCAT Svalbard radar observations of ionospheric plasma dynamics in relation to dayside auroral transients. *Journal of Geophysical Research*, *106*(A10), 21,453–21,461. https://doi.org/10.1029/2000JA000378

Ogawa, T., Buchert, S. C., Nishitani, N., Sato, N., & Lester, M. (2001). Plasma density suppression process around the cusp revealed by simultaneous CUTLASS and EISCAT Svalbard radar observations. *Journal of Geophysical Research*, *106*(A4), 5551–5564. https://doi.org/10.1029/2000JA900111

Oksavik, K., Barth, V. L., Moen, J., & Lester, M. (2010). On the entry and transit of high-density plasma across the polar cap. *Journal of Geophysical Research*, *115*, A12308. https://doi.org/10.1029/2010JA015817

Oksavik, K., Moen, J., & Carlson, H. C. (2004). High-resolution observations of the small-scale flow pattern associated with a poleward moving auroral form in the cusp. *Geophysical Research Letters*, *31*, L11807. https://doi.org/10.1029/2004GL019838

Oksavik, K., Moen, J., Carlson, H. C., Greenwald, R. A., Milan, S. E., Lester, M., et al. (2005). Multi-instrument mapping of the small-scale flow dynamics related to a cusp auroral transient. *Annales Geophysicae - Germany*, *23*(7), 2657–2670. https://doi.org/10.5194/angeo-23-2657-2005

Oksavik, K., Moen, J., Lester, M., Bekkeng, T. A., & Bekkeng, J. K. (2012). In situ measurements of plasma irregularity growth in the cusp ionosphere. *Journal of Geophysical Research*, *117*, A11301. https://doi.org/10.1029/2012JA017835

Oksavik, K., Moen, J. I., Rekaa, E. H., Carlson, H. C., & Lester, M. (2011). Reversed flow events in the cusp ionosphere detected by SuperDARN HF radars. *Journal of Geophysical Research*, *116*, A12303. https://doi.org/10.1029/2011JA016788

Oksavik, K., van der Meeren, C., Lorentzen, D. A., Baddeley, L. J., & Moen, J. (2015). Scintillation and loss of signal lock from poleward moving auroral forms in the cusp ionosphere. *Journal of Geophysical Research: Space Physics*, *120*, 9161–9175. https://doi.org/10.1002/2015JA021528

Rinne, Y., Moen, J., Oksavik, K., & Carlson, H. C. (2007). Reversed flow events in the winter cusp ionosphere observed by the European Incoherent Scatter (EISCAT) Svalbard radar. *Journal of Geophysical Research*, *112*, A10313. https://doi.org/10.1029/2007JA012366

Rino, C. L. (1979). Power law phase screen model for ionospheric scintillation.1. Weak scatter. *Radio Science*, *14*(6), 1135–1145. https://doi.org/10.1029/RS014i006p01135

Rodger, A. S., Pinnock, M., Dudeney, J. R., Baker, K. B., & Greenwald, R. A. (1994). A new mechanism for polar patch formation. *Journal of Geophysical Research*, *99*(A4), 6425–6436. https://doi.org/10.1029/93JA01501

Ruohoniemi, J., & Baker, K. (1998). Large-scale imaging of high-latitude convection with Super Dual Auroral Radar Network HF radar observations. *Journal of Geophysical Research*, *103*(A9), 20,797–20,811. https://doi.org/10.1029/98JA01288

Saito, Y., Yokota, S., Asamura, K., & Krieger, A. (2017). High-speed MCP anodes for high time resolution low-energy charged particle spectrometers. *Journal of Geophysical Research: Space Physics*, *122*, 1816–1830. https://doi.org/10.1002/2016JA023157

Skjaeveland, A. S., Carlson, H. C., & Moen, J. I. (2017). A statistical survey of heat input parameters into the cusp thermosphere. *Journal of Geophysical Research: Space Physics*, *122*, 9622–9651. https://doi.org/10.1002/2016JA023594

Southwood, D. J. (1987). The ionospheric signature of flux-transfer events. *Journal of Geophysical Research*, *92*(A4), 3207–3213. https://doi.org/10.1029/JA092iA04p03207

Spicher, A., Ilyasov, A. A., Miloch, W. J., Chernyshov, A. A., Clausen, L. B. N., Moen, J. I., et al. (2016). Reverse flow events and small-scale effects in the cusp ionosphere. *Journal of Geophysical Research: Space Physics*, *121*, 10,466–10,480. https://doi.org/10.1002/2016JA022999

Spicher, A., Miloch, W. J., Clausen, L. B. N., & Moen, J. I. (2015). Plasma turbulence and coherent structures in the polar cap observed by the ICI‐2 sounding rocket. *Journal of Geophysical Research: Space Physics*, *120*, 10,959–10,978. https://doi.org/10.1002/2015JA021634

Spicher, A., Miloch, W. J., & Moen, J. I. (2014). Direct evidence of double‐slope power spectra in the high‐ latitude ionospheric plasma. *Geophysical Research Letters*, *41*, 1406–1412. https://doi.org/10.1002/2014GL059214

Torrence, C., & Compo, G. P. (1998). A practical guide to wavelet analysis. *Bulletin of the American Meteorological Society*, *79*(1), 61–78. https://doi.org/10.1175/1520-0477(1998)079<0061:Apgtwa>2.0.Co;2

Valladares, C. E., Basu, S., Buchau, J., & Friischristensen, E. (1994). Experimental‐evidence for the formation and entry of patches into the polar‐cap. *Radio Science*, *29*(1), 167–194. https://doi.org/10.1029/93RS01579

van der Meeren, C., Oksavik, K., Lorentzen, D., Moen, J. I., & Romano, V. (2014). GPS scintillation and irregularities at the front of an ionization tongue in the nightside polar ionosphere. *Journal of Geophysical Research: Space Physics*, *119*, 8624–8636. https://doi.org/10.1002/2014JA020114

Van Dierendonck, A. J., J. Klobuchar, and Q. Hua (1993), Ionospheric scintillation monitoring using commercial single frequency C/A code receivers, paper presented at Proceedings of the 6th International Technical Meeting of the Satellite Division of The Institute of Navigation (ION GPS 1993), Salt Lake City, UT, September 22-24, 1993.

Wang, Y., Zhang, Q. H., Jayachandran, P. T., Moen, J., Xing, Z. Y., Chadwick, R., et al. (2018). Experimental evidence on the dependence of the standard GPS phase scintillation index on the ionospheric plasma drift around noon sector of the polar ionosphere. *Journal of Geophysical Research: Space Physics*, *123*, 2370–2378. https://doi.org/10.1002/2017JA024805

Wannberg, G., Wolf, I., Vanhainen, L. G., Koskenniemi, K., Röttger, J., Postila, M., et al. (1997). The EISCAT Svalbard radar: A case study in modern incoherent scatter radar system design. *Radio Science*, *32*, 2283–2307. https://doi.org/10.1029/97RS01803

Wernik, A. W., Pozoga, M., Grzesiak, M., Rokicki, A., & Morawski, M. (2008). Monitoring ionospheric scintillations and TEC at the Polish Polar Station on Spitsbergen: Instrumentation and preliminary results. *Acta Geophysica*, *56*(4), 1129–1146. https://doi.org/10.2478/s11600-008-0060-8